A Case Study of Wave–Current Interaction in a Strong Tidal Current

DIANE MASSON

Institute of Ocean Sciences, Sidney, British Columbia, Canada

(Manuscript received 6 December 1994, in final form 31 August 1995)

ABSTRACT

During August 1991, a field program was carried out in the vicinity of Cape St. James, off the British Columbia coast, where a strong tidally driven flow interacts with an active wave climate. Surface current maps were obtained from a CODAR-type HF radar (Seasonde) over an area of about 350 km^2 around the cape. A series of Loran-C drifters were also deployed during the experiment and used as ground truth for the radar. A comparison between the drifter and the radar surface currents indicates reasonable agreement.

Wave information was acquired with three Waverider buoys deployed around the cape. A significant modulation of the wave properties at the tidal period was observed for the buoy located in the area where the currents are maximum. The tidally induced changes in the wave field are modeled with a local wave–current interaction model based on wave action conservation and on a high-frequency limiting spectral shape. The model is applied on a period of 11 days for which the wind was relatively steady. The magnitude of the modeled tidal modulation of the wave field is of the same order of magnitude as the measurements but, in general, underestimates the measured tidally induced changes. However, during the first half of the period, the modulation of the total wave energy is significantly out of phase with the buoy data. The effect of refraction by the current on the waves is assessed using a backward ray tracing method and two-dimensional surface current maps. It is proposed that refraction effects are important during the first part of the study period and are a plausible cause for the phase discrepancy between the measurements and the results of the local model.

1. Introduction

When ocean waves propagate through a spatially varying current, their properties can be significantly affected. A striking example is provided by waves encountering strong tidal currents. It has been shown that these waves exhibit some modulation of their properties at the tidal period (e.g., Gonzáles 1984; Tolman 1991). The magnitude of such changes in the wave field is of crucial importance in many engineering applications (e.g., Hedges 1987) as well as posing a navigational hazard. Wave–current interaction has been proposed as a possible mechanism for the formation of giant waves known to occur in strong coastal currents (e.g., Smith 1976; Irvine 1987). On the Canadian Pacific coast, the waters around Cape St. James, located at the southern tip of the Queen Charlotte Islands (Fig. 1), are known by local navigators for their dangerously heavy seas. For example, in October 1968, during an intense North Pacific storm, an oil-drilling rig anchored in the vicinity of the cape was hit by an enormous wave of 29-m height, propagating against a strong local ebb current (James 1969).

Although the influence of surface currents on ocean waves have long been known, detailed quantitative measures of this phenomenon are rather scarce. In part, this deficiency is due to the difficulties of in situ monitoring of the waves as well as of the underlying surface current field. Consequently, many of the existing studies on wave–current interaction in the ocean have been based solely on data from remote sensing instruments in order to obtain an adequate spatial coverage, as in Liu et al. (1994) and Irvine and Tilley (1988). Wang et al. (1994) recently examined the change in directional wave spectra recorded by a pitch–roll buoy induced by a Gulf Stream meander. However, in this study there was no direct measure of the Gulf Stream current; changes of water temperature at the buoy were used as an indication of the presence or absence of the Stream. Gonzáles (1984) and Tolman (1991) both present observations of the modulation of wave properties by the tidal current, but again, no direct observations of the currents were available.

To complement the limited field data available on wave–current interaction, a field program was carried out during August 1991 in the vicinity of Cape St. James (Fig. 1). This area was chosen because of the ideal conditions for wave–current interaction: swell from the Pacific as well as local wind waves encounter a vigorous tidally driven flow. Surface cur-

---

Corresponding author address: Dr. Diane Masson, Institute of Ocean Sciences, P.O. Box 6000, 9860 West Saanich Rd., Sidney, BC V8L 4B2, Canada.
E-mail: mdia@ios.bc.ca

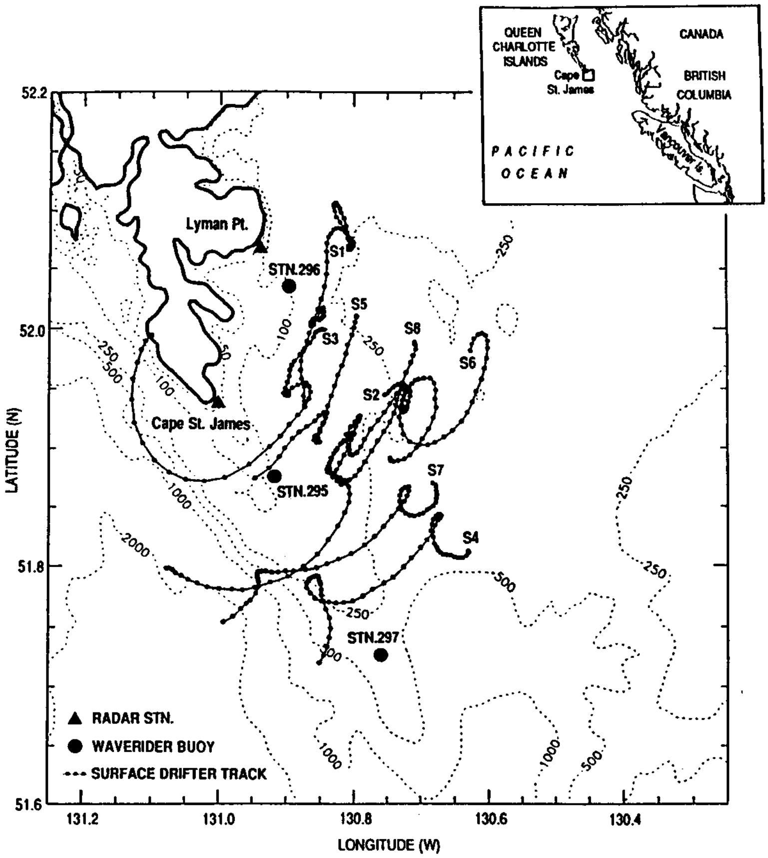

FIG. 1. The study area with the location of the wave buoys ●, the radar stations △, and the eight surface drifter tracks —•—•—•—. The track numbers (S1–S8) have been placed at the location of the respective launches. Depth contours are in given in meters.

rent data were collected using a high-frequency (HF) radar, the Seasonde, which can map surface currents over a fairly large area. A series of Lagrangian surface drifters were also used to establish the reliability of the radar. The wave field was monitored by three Waverider buoys.

The field program is described in the following section. A comparison between radar and drifter surface current is performed in order to give confidence in the radar current measurements. Data from a Waverider buoy located in the area of maximum tidal current indicate a strong modulation of wave properties at the tidal period. In section 3, time series of the surface current measured at the buoy location are used by a local model, based on wave action conservation, to simulate variations of the spectral wave properties. In this model, the high-frequency tail of the spectrum is limited to an equilibrium-type shape. Finally, the effects of refraction by the horizontal shear of the current on the wave field are evaluated by using a backward ray tracing method.

2. Field program

The Cape St. James area is known as one of the windiest regions of Canada. The coastal winds tend to blow parallel to the coast, predominantly from the northwest during the summer months. A time series of wind vectors recorded at the cape weather station is given in Fig. 2 for the period of the field program (7–25 August 1991). The wind is measured at 90 m above sea level and brought down to the standard 10 m following the iterative method of Smith (1988) based on the Charnock wind stress formula and assuming neutral atmospheric stability. During the field program, a moderate wind was typically blowing from the northwest, except for the beginning of the study when a storm system with high winds from the south-southeast passed through the area. Also, for a several day period near the end, the wind shifted to the southwest.

a. Surface current measurements

The strong tidal currents around the cape are mixed but predominantly semidiurnal. In addition, a persistent

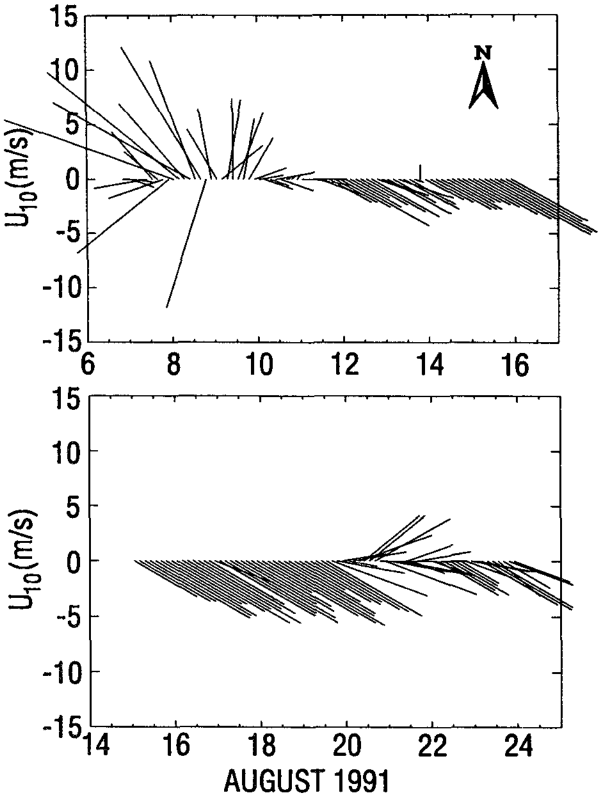

FIG. 2. Wind vector at a 10-m height, U_{10}. The vectors indicate the direction in which the wind is blowing.

surface outflow into the Pacific has been identified within 20 km of the cape (Crawford et al. 1994). A CODAR-type HF radar, the Seasonde, was used to measure the surface current around the cape. This instrument measures current velocity from the first-order echo scattered by Bragg reflection from ocean waves of wavelength equal to one-half of the HF signal wavelength. The 12-MHz radar signal is scattered by short deep water waves of 0.36-Hz frequency. The transmitted signal is Doppler shifted by the surface waves advected by the near-surface current. If a linear vertical profile of the current is assumed, it can be shown that the radar probes the current at a depth of approximately 8% of the wavelength of the waves, or about 1-m depth in the present study (Teague 1986). The radar deduces the component of the surface current along the line between the waves and the radar from the difference between the total Doppler shift measured by the radar and the one due to the phase velocity of the waves alone. Two sites are required to construct a map of total current vectors from radial components measured at both radar locations. The current can then be estimated in the overlap region of the two radar units. The integrity of the deduced vector maps is, however, limited to an area where the radial components from the two radars intersect at a large enough angle. Therefore, one has to limit the analysis to the region where the vector estimate is reasonably stable (Leise 1984).

In this experiment, two radar units operated continuously while the average radial files at each location were archived every 60 minutes (see Fig. 1 for locations of the two units). The combined current vectors were computed over a 1 km × 1 km grid using a 5-km averaging radius. In Fig. 3, an example of the two radial maps is given, along with the resulting current map covering an area of about 350 km^2.

Eight surface drifters employing Loran-C navigation and drogued at a mid-depth of 2.5 m were deployed in the study area from 21 to 24 August. Each unit relayed its position every 30 minutes to a standby vessel by VHF radio telemetry. The drift tracks are shown in Fig. 1. All the drifters traveled in a south-southwest direction, consistent with a strong southward residual current. The tracks also indicate a maximum current of about 2 m s^{-1} just south of the Cape near STN295.

Given the experimental nature of the radar unit, a detailed comparison of the drifter and radar surface current estimates was performed. For each pair of successive drifter positions within the radar current vector grid, the mean velocity of the drifter was computed from the distance traveled and the elapsed time (30 minutes). For a midpoint and a midtime between the two positions, the radials from the two radar stations were used to estimate the surface current measured by the radar. To do so, the two radial maps measured at times just before and after the mid-drifter time were used. A total of 226 points were analyzed from five different drifter tracks. The two sets of surface current estimates are in reasonably good agreement for all stages of the tidal cycle (Fig. 4). This successful comparison demonstrates the reliability of the radar for the present field conditions.

b. Wave data

At the onset of the field program, three Waverider buoys (0.9-m diameter) were deployed in water depths of 115 m (STN295), 185 m (STN296), and 290 m (STN297) (Fig. 1). STN295 was located about 10 km southeast of the cape where the tidal currents are known to reach a local maximum. The second buoy, STN296, was deployed southeast of Lyman Point where one of the two radar units was operating. Finally, STN297 was located approximately 30 km to the southeast of Cape St. James outside of the strong tidal current regime that characterizes the region around the cape. The mooring lines were designed in such a way that the buoys would perform satisfactorily in the strong current (up to 2.5 m s^{-1}). The wave buoys recorded for 27 minutes every half-hour at a sampling rate of 1.28 Hz for the whole period, except for the buoy at STN296, which ceased to function

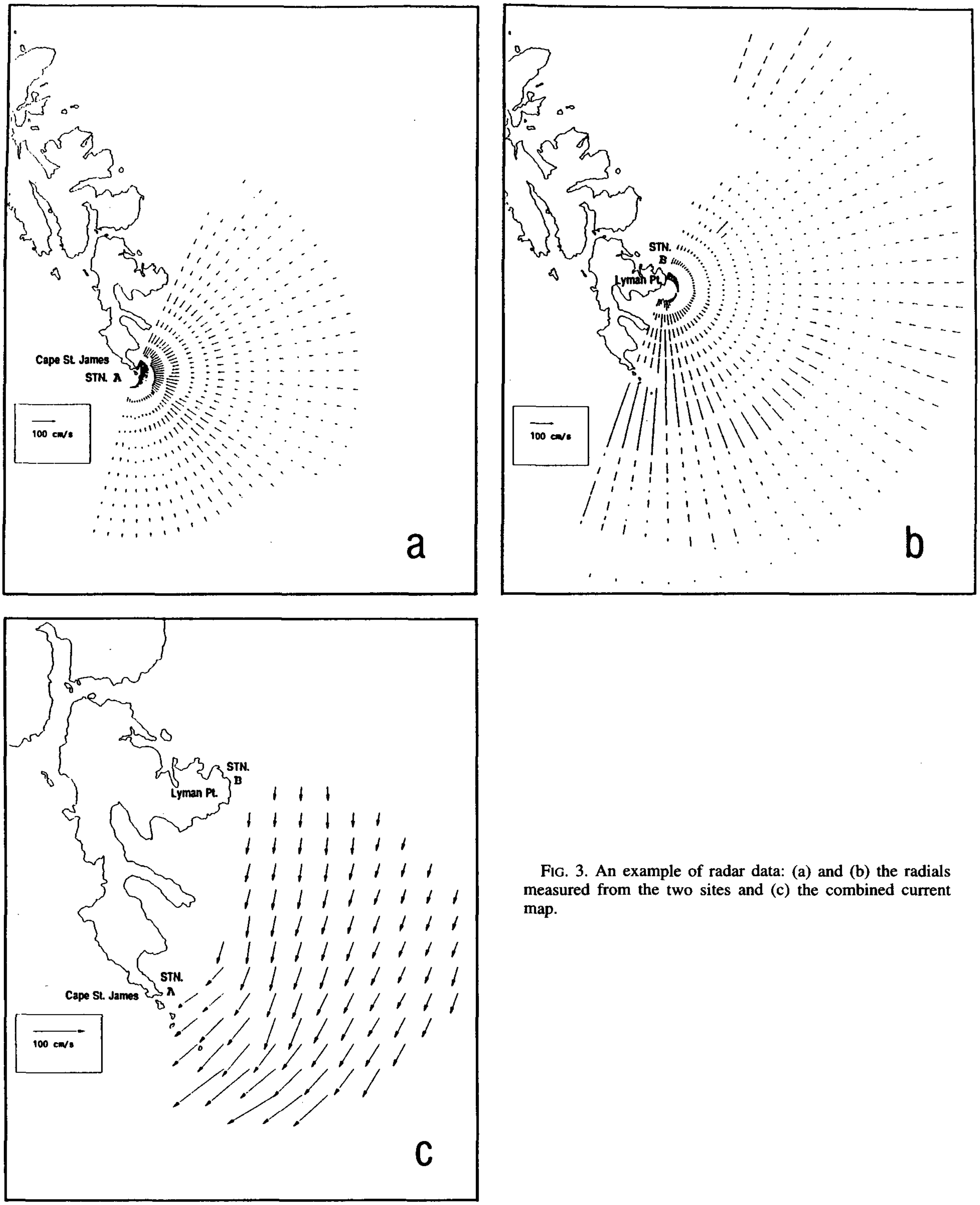

FIG. 3. An example of radar data: (a) and (b) the radials measured from the two sites and (c) the combined current map.

properly on 14 August. For each half-hour, a fast Fourier transform was applied to the time series of the heave signal using a Hanning window with 50% overlap to give a frequency spectrum with a bandwidth of 0.005 Hz and about 16 degrees of freedom. The spectral data were then reprocessed to average over two

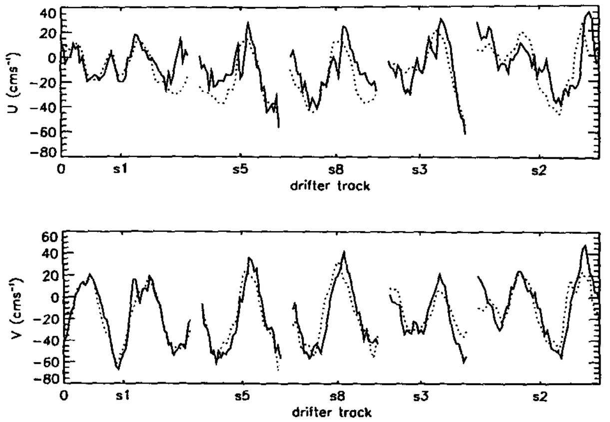

FIG. 4. Surface current speed measured by the drifters (full line) and by the radar (dotted line). The measurements are located along the segments of five drifter tracks located in the area covered by the radar: U is the east–west component of the velocity, and V the north–south one.

frequency bands to give an average bandwidth of 0.01 Hz and 32 degrees of freedom.

The first three moments of the frequency wave spectra derived from the buoy measurements were computed as

$$m_r = \int_0^\infty \omega^r E(\omega)\,d\omega, \quad \text{for} \quad r = 0, 1, 2, \qquad (1)$$

with ω the radial frequency and $E(\omega)$ the frequency power spectrum. From these spectral moments, the significant wave height, $H_s = 4\sqrt{m_0}$ (Fig. 5), and the spectral bandwidth, $\nu = (m_2 m_0/m_1^2 - 1)^{1/2}$ (Fig. 6), were computed for each 30-minute period.

In the time series of H_s, the most striking feature is the signature of the storm (7–9 August) during which the significant wave height increased to about 6 m for the three buoys. After the storm, the H_s values remain relatively low with a slightly lower value for STN296, which is in the lee of the cape for the northwest wind. Also evident in Fig. 5 is the strong semidiurnal oscillation of the wave energy. This 12-hour signal is most pronounced at STN295, which is located in the area of maximum tidal current. At times, the wave energy level is highly dominated by the tidally induced variations, with changes in H_s of up to 50%.

Over the whole measurement period, the spectral bandwidth of Fig. 6 has a mean value around $\nu = 0.5$. By comparison, the spectral bandwidth of a typical JONSWAP spectrum would be around[1] $\nu = 0.4$. However, there are episodes where the parameter ν assumes significantly larger values, with $\nu \geqslant 0.6$, because of the bimodal nature of the local spectrum, which is then composed of a low-frequency swell from the Pacific and of a high-frequency local component. The tidally induced variation is also present in the spectral bandwidth data of Fig. 6. Again, the tidal signal is much more pronounced at STN295 and is particularly evident during the second half of the field program.

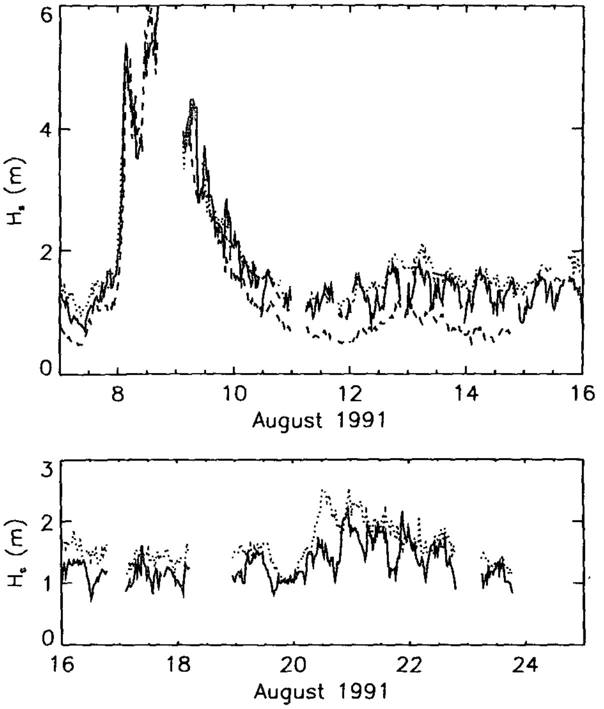

FIG. 5. Significant wave height H_s for the three Waveriders: STN295 (full line), STN296 (dashed line), and STN297 (dotted line).

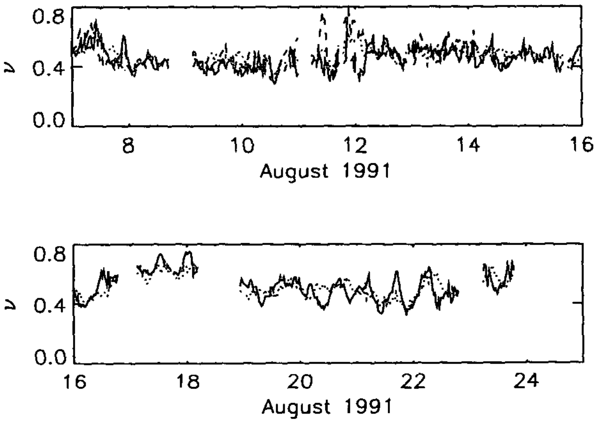

FIG. 6. As in Fig. 5 but for spectral bandwidth ν.

---

[1] In the calculation, the peak frequency is 0.1 Hz, the value of the spectral peak enhancement factor takes the typical value of $\gamma = 3.3$, and the cutoff frequency used is consistent with the data—i.e., 0.64 Hz.

3. Wave–current interaction model

The wave measurements near the cape (STN295) show a strong tidal modulation of both the wave energy and spectral shape. Given the nature of the tidal current measured by the radar, how well can one model these changes? The way in which waves and current are known to interact depends on the incident directional wave field and on the two-dimensional structure of the surface current. However, in many cases, it may be possible to obtain a reasonable approximation of the interaction by using a local model based on wave action conservation, in which deep water waves enter a region of uniform current from quiescent water. The results from this first approach are presented in section 3a. One serious drawback from this simple model is that, for an opposing current, the theory predicts an unlimited growth of the high-frequency wave components. These short waves are bound to be limited in their growth either by reflection or breaking due to excessive steepness. A correction for this effect is introduced in section 3b. The results of sections 3a and 3b are then combined to construct a local wave–current interaction model. The wave spectral properties measured in the strong current at STN295 are then compared with predictions from this local model. Finally, the model is modified to include the refraction of the waves by horizontal shear in the current. This is done by using a backward ray tracing technique in which wave rays are traced from a point in the current back into an area where the surface currents are much weaker and the wave field known (section 3d).

a. Local model: Wave action conservation

The changes in the wave field as it propagates into a surface current are modeled here by decomposing the wave field into a series of purely harmonic components, which implies that the amplitude of each component is assumed small compared to its wavelength. Also, the time and length scales of the current are assumed to be much larger than the period and wavelength of the waves. These assumptions allow the problem to be described within the framework of linear wave theory. The second assumption also allows one to consider the wave properties anywhere in the current to be the same as those of a plane wave on a uniform current. The sea surface displacement at any position $\mathbf{x}$ and time t can then be expressed as the sum of components of angular frequency ω_n and wavenumber $\mathbf{k}_n$:

$$\eta(\mathbf{x}, t) = \mathrm{Re}\Big(\sum_n c_n e^{i(\mathbf{k}_n\cdot\mathbf{x} - \omega_n t + \epsilon_n)}\Big) \qquad (2)$$

with c_n the amplitude and ϵ_n a random phase. For waves propagating on a surface current, $U(\mathbf{x}, t)$, the angular frequency is obtained as

$$\omega = \mathbf{k}\cdot\mathbf{U}(\mathbf{x}, t) + \sigma, \qquad (3)$$

where the intrinsic frequency, σ, and the wavenumber are related by the linear dispersion relation. Because of the relatively large depth of the study area, the problem is simplified by using the deep water approximation to the dispersion relation,

$$\sigma^2 = gk, \qquad (4)$$

where g is the gravitational acceleration.

We are seeking a model that would allow us to compute changes in the wave field as the waves propagate onto a varying current $\mathbf{U}(\mathbf{x}, t)$. For each frequency component n of (2), the wave energy density, $E = \rho g c_n^2/2$, is governed by the action conservation principle (e.g., Phillips 1980)

$$\frac{\partial A}{\partial t} + \nabla\cdot[(\mathbf{U} + \mathbf{c}_g)A] = 0, \qquad (5)$$

where the deep water group velocity is obtained from (4),

$$\mathbf{c}_g = \frac{\partial\sigma}{\partial k}\frac{\mathbf{k}}{k} = \frac{1}{2}\left(\frac{\sigma}{k}\right)^{1/2}\frac{\mathbf{k}}{k},$$

and the wave action density is $A = E/\sigma$. A practical approach is to estimate changes in the power spectral density, say $E(\omega)$ for a unidirectional wave field, which, for each component of (2), is $E(\omega_n) = c_n^2/2\delta\omega$, with $\delta\omega$ the spectral increment. Because the timescale of change associated with the local current is much longer than the period of the waves, the current can be considered as steady with, in (3), $\mathbf{U}(\mathbf{x}, t) \equiv \mathbf{U}(\mathbf{x})$. Then, for a steady state, the kinematic conservation law of waves implies that the frequency ω is invariant. Under these conditions, (5) gives an expression for the spectral density of each wave component

$$\nabla\cdot\left[(\mathbf{U} + \mathbf{c}_g)\frac{E(\omega)}{\sigma}\right] = 0. \qquad (6)$$

Huang et al. (1972) used (6) to derive spectral changes in a simple one-dimensional case where all the waves travel in the same direction from a region of quiescent water into a uniform nondivergent current with component U parallel to the waves. The spectral density in the current, $E_1(\omega)$, becomes in terms of the incident spectrum, $E_0(\omega)$

$$E_1(\omega) = \begin{cases} E_0(\omega)\dfrac{4}{\left[1 + \left(1 + \dfrac{4U\omega}{g}\right)^{1/2}\right]^2\left(1 + \dfrac{4U\omega}{g}\right)^{1/2}}, & \text{if } 4U\omega/g > -1 \\ 0, & \text{otherwise,} \end{cases} \qquad (7)$$

where U is the current velocity parallel to the waves. According to this model, waves propagating into a following current lengthen and their amplitudes are reduced. Conversely, waves entering an opposing current are shortened with their amplitudes increased. In the latter case, a relatively strong opposing current can cause the shorter wave components to be *blocked,* with $4U\omega/g \leqslant -1$. This is because the upstream group velocity is smaller than the current velocity and the transport of wave energy is blocked. In practice, those short waves will either be reflected or will break before reaching the blocking point, and the spectral levels should follow some kind of limiting form.

b. High-frequency tail

In an opposing current, the application of the model of the previous section results in high energy levels for frequencies just below the blocking point followed by an abrupt energy drop to zero at the blocking point. An unrealistic overshoot of energy then develops just below the cutoff frequency. Kitaigorodskii et al. (1975) examined the problem of an equilibrium spectral range in the case of surface waves on a uniform current. Their approach was based on the principle, first suggested by Phillips (1958), of a universal shape for the wavenumber spectrum in the equilibrium range of a wind wave spectrum. Based on the idea of a saturation range where the wave energy is limited by breaking, Phillips (1958) derived, on dimensional grounds, a wavenumber spectrum, $\Psi(\mathbf{k})$, of the form

$$\Psi(\mathbf{k}) = Bk^{-4}G(\theta), \qquad (8)$$

where B is a nondimensional constant, and $G(\theta)$ the normalized angular spreading function. Assuming that, in the case of a uniform current, the wavenumber spectrum still has an equilibrium range of the universal shape, Kitaigorodskii et al. (1975) derived an expression for the equivalent frequency spectrum

$$E(\omega) = \int_{-\pi}^{\pi} \frac{\Psi(\mathbf{k})k}{\partial\omega/\partial k}\, d\theta, \qquad (9)$$

using the dispersion relation (3) to estimate the factor $\partial\omega/\partial k$ and with the wavenumber spectrum $\Psi(\mathbf{k})$ given by (8). Hedges et al. (1993) made some estimates of wave spectral changes by large-scale currents using an equilibrium range formulation based on (8).

More recently, the nature of the equilibrium range was reexamined by Phillips (1985), who found the hypothesis of a fixed upper limit asymptote to the spectrum no longer tenable. He suggested instead an equilibrium range in which all source terms are important in the energy balance, resulting in a new wavenumber spectral form

$$\Psi(\mathbf{k}) = \beta u_{*} g^{-1/2} k^{-7/2} G(\theta), \qquad (10)$$

where β is a constant and u^* the friction velocity. Following Kitaigorodskii et al. (1975), one can use the equilibrium form of (10) and, assuming that the nature of the equilibrium for the wavenumber spectrum also prevails in a uniform current, derive a modified expression for the frequency spectrum of the form

$$E(\omega) = \alpha u_{*} g \omega^{-4} J(\mathbf{U}, G(\theta)), \qquad (11)$$

with

$$J(\mathbf{U}, G(\theta)) = \frac{1}{2g^{3/2}} \int_{-\pi}^{\pi} \omega^4 k^{-5/2} G(\theta) \Bigg/ \left(\frac{1}{2}\left(\frac{g}{k}\right)^{1/2} + \frac{\mathbf{k}\cdot\mathbf{U}}{k}\right) d\theta. \qquad (12)$$

According to (12), the equilibrium frequency spectrum does not exactly follow a simple power law as in the case of no current because of the current-induced Doppler effect represented by the correction factor $J(\mathbf{U}, G(\theta))$. Here, this function is evaluated numerically for two forms of the directional function $G(\theta)$: a $\cos\theta$ and a $\cos^2\theta$ (Fig. 7). As previously noted by Kitaigorodskii et al. (1975), a following current results in a slight decrease in the slope of the frequency equilibrium spectrum, and to a corresponding increase for an opposing current. Also in agreement with Kitaigorodskii et al. (1975), the results of Fig. 7 indicate a slight increase of the effect of the current on the spectral shape as the spectrum narrows.

c. Local model versus data

The equilibrium range spectral form (11) combined with the spectral transform (7) are used to construct a local wave–current interaction model to simulate the tidally induced variability of wave spectral properties measured at STN295. An hourly time series of the surface current at this location is first extracted from the radar data (Fig. 8).

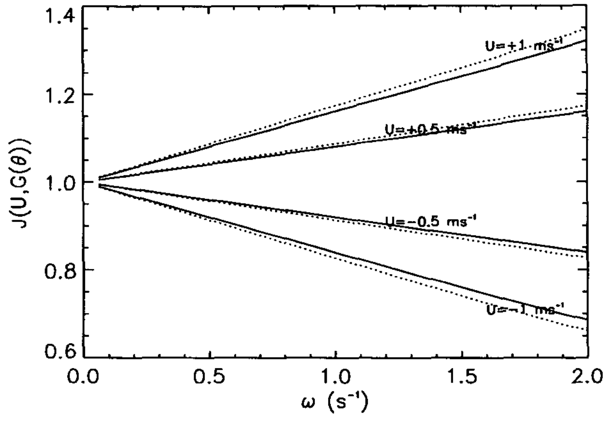

FIG. 7. Correction factor $J(\mathbf{U}, G(\theta))$ for spreading function $G(\theta)$ of the $\cos\theta$ (full line) and $\cos^2\theta$ (dotted line) type.

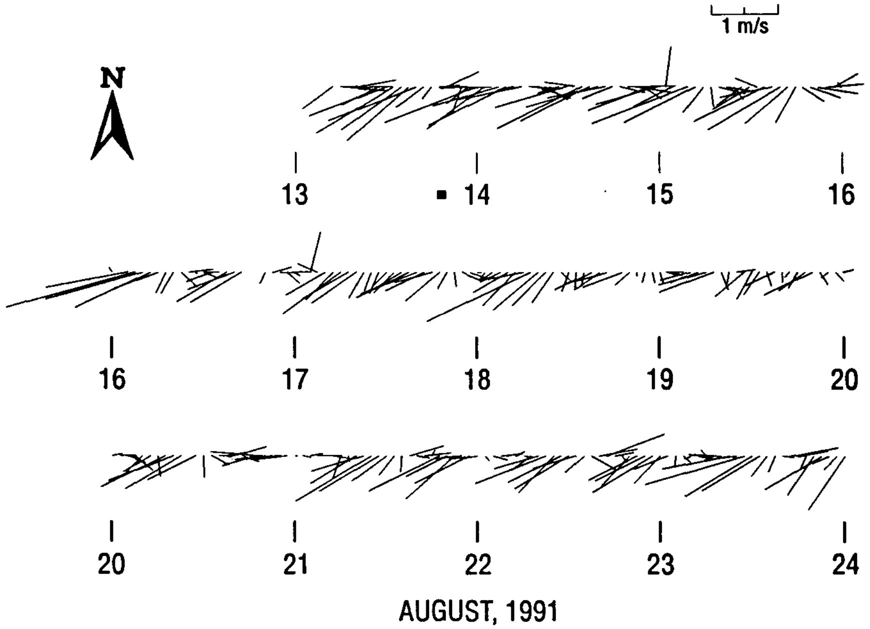

FIG. 8. Hourly surface current vectors measured by the radar at STN295.

The 11-day interval, 13–24 August, was chosen for the analysis, during which time radar data are available and the wind conditions remained relatively steady at the cape as well as in the region surrounding it. The vector plot of surface current measured at STN295 (Fig. 8) shows a succession of periods of strong ebb current flowing in the southwest direction followed by periods of weaker flood current in the opposite direction. This asymmetry in the tidal flow is caused by the strong southward residual current previously mentioned.

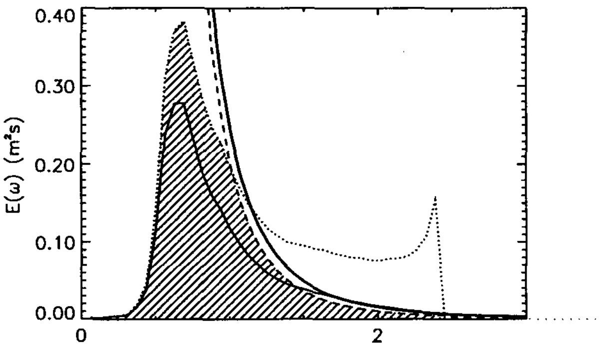

FIG. 9. Mean frequency spectrum at STN297 for the interval 13–24 August (thin full line). The same spectrum interacting with a current $U = -1$ m s^{-1} according to (7), $E_1(\omega)$ (dotted line). The equilibrium range spectral parameterization of (11) in the opposing current (dashed line) and the final spectrum (shaded area). The equilibrium range with $U = 0$ is also given as the thick full line.

A mean spectrum computed over the whole period from the STN297 buoy data (Fig. 9) is used as a constant incident spectrum [$E_0(\omega)$ in (7)]. The measurements at STN297 are used because this buoy was located outside of the area of strong tidal currents, which is known to be within about 20 km from the cape, and consequently represents a good approximation of the mean incident wave field. Over the 11-day interval, variations of the wave spectrum at STN297 about the mean values of Fig. 9 are relatively small compared to the spectral changes measured at STN295 (see Figs. 5 and 6). The only exception is the occurence of a very low frequency swell during 16–18 August, which is reflected in a marked increase of the spectral bandwidth at the two buoys (Fig. 6). However, because of its very low frequency (0.8 Hz), this swell is barely affected by the tidal current and does not affect the following results. Hourly time series of wave spectra were initially used as input to the local model. However, the use of a long-term mean spectrum as input to the local model was chosen as more representative of the *untouched* incident spectrum than the actual measured time series of spectra. This was done because, although the current is much weaker at STN297 than at STN295, it is nonzero. In fact, there is a small but clear tidal modulation of the high-frequency wave energy measured by the buoy at STN297.

For each hourly interval, the surface current from the radar is used to modify the input spectrum following (7). An example of this transformation is given in Fig. 9 where an opposing current of $U = -1$ m s^{-1} is used as local current. The overshoot of energy is evident just below the cutoff frequency $\omega = -g/4U = 2.45$ s^{-1}.

Because there were no direct measurements of wave direction, the component of the surface current parallel to the mean direction of the waves, U, is obtained by assuming that the waves travel in the wind direction for the whole period. The parameter U is then simply the component of the measured current vector along the wind direction. This assumption is reasonable given that both the local sea, which must propagate along a direction close to that of the wind, and the swell must be coming from the open ocean, that is, from a sector extending from about 225 to 300 degrees True (see Fig. 1). Within this southwest–west-northwest quadrant, small variations of the incident wave direction would not affect the results of this local model significantly given the nature of the local current, which travels dominantly along a southwest–northeast line. The magnitude of the tidal modulation could vary moderately, but not its phase. In section 3d, the effect of changes in the wave direction will be examined when refraction is considered.

The resulting spectrum, $E_1(\omega)$, is corrected in the equilibrium range using (11). To do so, the following assumptions are made.

- The spreading function in the equilibrium range follows $G(\theta) \propto \cos^2(\theta)$.
- The friction velocity is obtained from the standard relation $u_* = \sqrt{C_d} U_{10}$ with the drag coefficient $C_d = 0.001$ and the wind speed at 10 m given a mean value $U_{10} = 8$ m s^{-1}.
- The constant α takes a midvalue within the possible range $\alpha = 0.1$ (see Phillips 1985).

The equilibrium spectral values are plotted in Fig. 9 for the case $U = -1$ m s^{-1} and indicate a smooth decay of wave energy within the equilibrium range. Also shown in Fig. 9 is the equilibrium range spectrum for the zero current case for which the correction factor (12) is unity, $J(\mathbf{U}, G(\theta)) \equiv 1$. The very good agreement of the latter with the mean spectrum measured by the buoy at frequencies away from the peak supports the Phillips equilibrium range formulation.

In the following calculations, the spectral shape is limited by the equilibrium form for all frequency components where the uncorrected spectral density $E_1(\omega)$ exceeds that given by (11). The final wave spectrum is indicated in Fig. 9 by the shaded area. Using the above procedure, a transformed spectrum is obtained at each hour period for which the radar data provided a valid current vector for the STN295 location. A total of 256 spectra are computed for the 11-day interval, and the results are summarized in Fig. 10. From the time series of transformed spectra, the time evolution of the significant wave height H_s spectral bandwidth ν and energy content at high frequencies, E_{ER}, have been estimated. The latter is simply the integral of the spec-

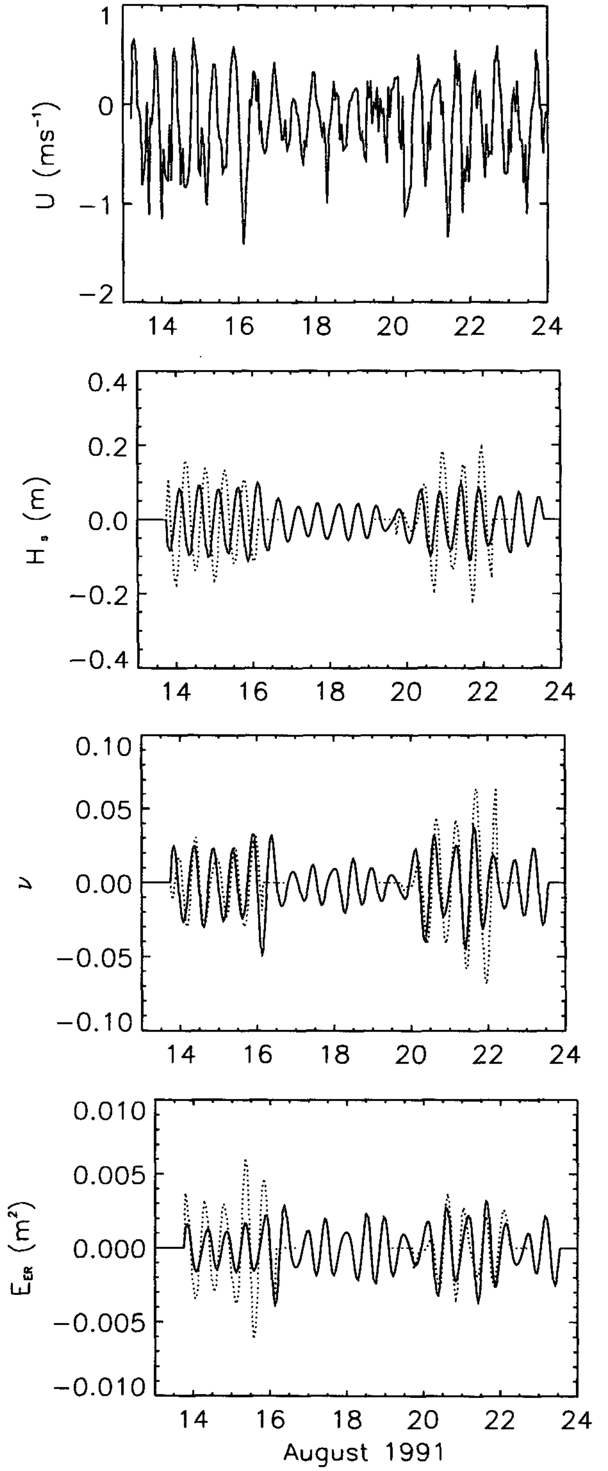

FIG. 10. Time series of surface current parallel to the waves, U, measured by the radar at STN295 (a). The computed variations at the tidal period (9–15 h), for H_s (b), ν (c), and E_{ER} (d). The Waverider data (dotted line) and the local model results (full line) are given.

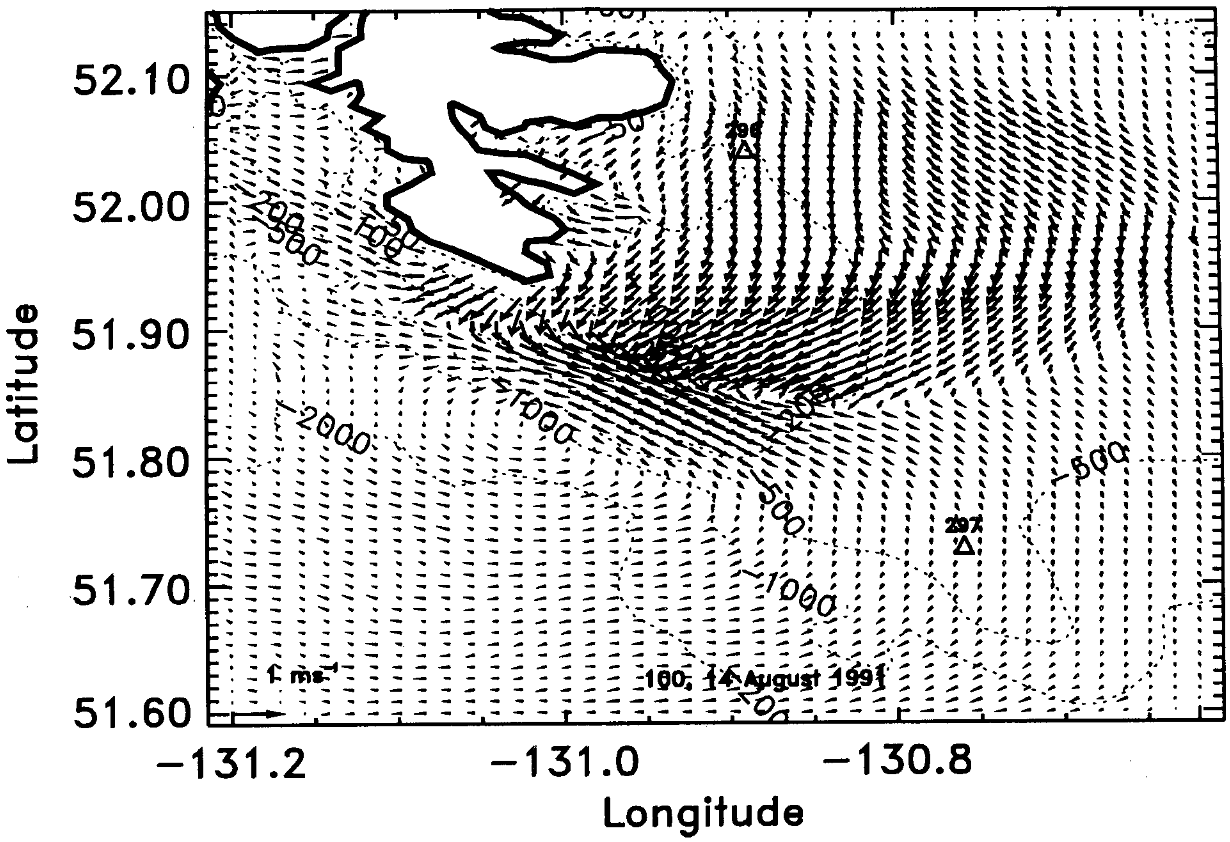

FIG. 11. Map of surface current around Cape St. James. The grid is 40 km × 60 km on which the current vectors are obtained from the radar data and the output of a tidal model.

trum over a range of frequencies for which $\omega \geqslant 2\omega_p$, where ω_p is the frequency of maximum spectral density. These three spectral parameters were also obtained for the spectra measured at STN295 by the Waverider buoy. In order to compare the model predictions of the tidally induced variations of the wave field with the measurements, the time series of the spectral parameters are first bandpassed around the dominant tidal frequency with a range of periods of 9–15 h. This period interval contains most of the energy of the measured surface current.

As seen in Fig. 10a, the component of the surface current parallel to the waves, U, follows a strong 12-h modulation. The incident wave field encounters episodes of moderate following current (<1 m s^{-1}) followed by periods of stronger opposing current reaching speeds of up to 1.5 m s^{-1}. Accordingly, the model predicts a decrease of the wave energy, or H_s, in following current and an increase of energy in opposing current as the wave components near the spectral peak, where most of the wave energy resides, simply follows the wave action conservation law of (7). Figure 10b indicates the tidal modulation of H_s for the model and the measurements. The amplitude of the modulations is in reasonable agreement with the measured tidally induced changes although the model, in general, underestimates the variations, especially during the second half of the study. However, the phase of the local model clearly disagrees with the measurements in the first part of the analysis period during which the buoy data indicate energy maxima and minima that do not correspond with the periods of extreme opposing and following currents. For the second half of the interval (19–22 August), the phase of the predicted changes in wave energy of the local model are much closer to the measurements. It is interesting to note that, during the latter period, the wind had shifted slightly and was now blowing from the southwest (Fig. 2). In the next section, the importance of refraction on the model's prediction will be evaluated.

The tidally induced changes of the spectral bandwidth ν predicted by the local model are generally close to the measured ones (Fig. 10c) with, again, an underestimation of the modulations during the second half. During episodes of opposing current the spectrum narrows significantly while it is broadened in a following current. This can be better understood by looking at variations in the high-frequency content of the spectrum, E_{ER}, which strongly controls the changes in spectral bandwidth. When the short waves encounter a strong adverse current, they steepen to a point where their growth is limited either by excess breaking or by reflection. In the model, this limitation is represented by the spectral form of Eqs. (11) and (12). This results in a severe restriction on the high-frequency content of the spectrum. Therefore, the tidally induced variations of the high-frequency part of the spectrum are completely out of phase with the main part of the spectrum. This spectral behavior for the short waves predicted by the local model appears to be in good agreement with the buoy data (Fig. 10d), which indicate strong tidally induced modulations of 25%, which are also out of phase with the parameter U and in phase with the measurements. But, as for H_s, the model underestimates the amplitude of the modulations during the first interval. A similar behavior of the high-frequency content of a wave spectrum in opposing current was obtained in laboratory experiments by Suh et al. (1994), who observed lower high-frequency wave energy in opposing current.

d. 2D refraction: Backward ray tracing

Current-induced changes in the waves have been modeled by a simple local approach where the incident waves are assumed to travel from quiescent water into a uniform current. During the first half of the studied interval, the results of the local model, which do not include refraction, were quite different from the measurements, with a significant phase lag between predicted and measured modulation of the wave energy (Fig. 10b). In the following, we investigate how refraction can affect the time evolution of the local wave energy.

The sea surface displacement (2) can be represented by a continuous spectrum of plane wave components with wavenumber vector $\mathbf{k}$, denoted $\Psi(\mathbf{k})$. It can be shown that, neglecting external sources of wave action, the spectral density of wave action in the wavenumber domain, $N(\mathbf{k}) = \Psi(\mathbf{k})/\sigma$, remains conserved along a ray (e.g., Phillips 1980, p. 182). The rays are curves along which the wave energy propagates. The ray paths are calculated according to the standard ray equations in finite water depth h and stationary current:

$$\frac{d\mathbf{r}}{dt} = \mathbf{U} + \mathbf{c}_g, \tag{13}$$

where $\mathbf{r}$ is the coordinate along the ray path and

$$\frac{d\mathbf{k}}{dt} = -(\nabla\mathbf{U})\cdot\mathbf{k} - \left(\frac{\partial\sigma}{\partial h}\right)\nabla h. \tag{14}$$

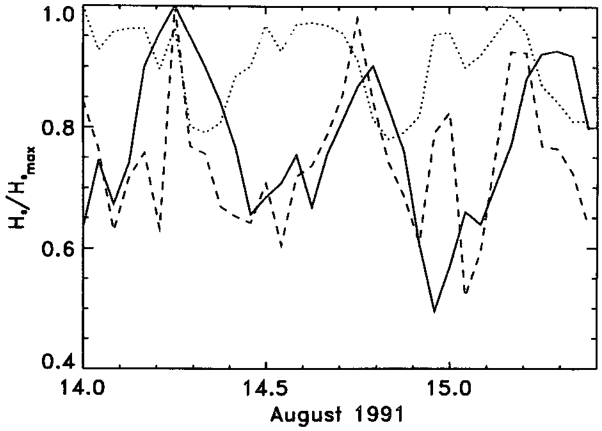

FIG. 12. Significant wave height H_s normalized by the maximum value during the 33-h interval, $H_{s_{\max}}$. The three curves are the measurement at STN295 (full line), the results of the local model (dotted line), and the results of the backward ray tracing method (dashed line).

To transform the spectral action density conservation law from the wavenumber to the frequency and direction spectral domain, the Jacobian is derived from the relation

$$\Psi(\mathbf{k})kdkd\theta = F(\omega, \theta)d\omega d\theta. \tag{15}$$

Using (15), the directional frequency spectrum can be shown to obey

$$\frac{d}{dt}\left(\frac{F(\omega, \theta)}{\sigma}\frac{\partial\omega}{\partial k}\frac{1}{k}\right) = 0, \tag{16}$$

where d/dt denotes differentiation along a ray path. The dispersion relation (4) is replaced by one valid in finite water depth

$$\sigma^2 = gk\tanh(kh). \tag{17}$$

By tracing the rays backward from a point in the current, the wave spectral value for each spectral component at this location can be estimated from the corresponding spectral value of a known incident spectrum. The full directional spectrum at a location in the current can then be reconstructed by summing the contributions of each spectral component. This backward ray tracing method is used here to estimate tidally induced variations in the directional wave field at STN295. The incident spectrum is again taken as the mean spectrum at STN297, with a directional spreading function of the form $G(\theta) \propto \cos^2(\theta)$. The spectral space is discretized into 60 frequency bands and 360 direction bands. The integration is done with the fourth-order Runge–Kutta method.

As for the one-dimensional spectrum, the directional spectrum in the equilibrium range is adjusted to follow the form of (10). Using (15), this spectral form becomes, in the frequency and direction domain,

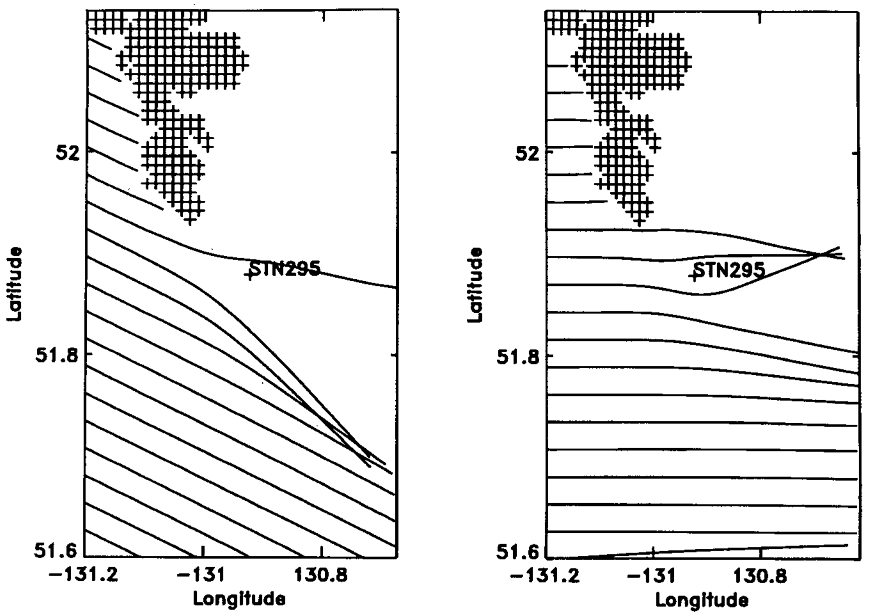

FIG. 13. Ray paths for waves from the northwest (a) and from the west (b).

$$F(\omega, \theta) = \frac{\beta u_{*} g^{-1/2} k^{-5/2} G(\theta)}{\partial \omega / \partial k}, \qquad (18)$$

with $\beta = \alpha/2$. To obtain (18), the directional spreading function is assumed to be the same in both wavenumber and frequency/direction spectral domains. In the model, the spreading function directly obtained from the backward ray tracing method for each frequency is used in the equilibrium range formulation (18) as $G(\theta)$. Then the energy levels are corrected, as was done in the 1D model, by limiting spectral values to the results of (18) whenever the energy levels predicted by (16) exceed those values.

For a 40 × 60 km^2 area close to the cape, hourly surface current maps were obtained on a 1 km × 1 km grid for a 33-hour interval, from 0000 UTC 14 to 0900 UTC 15 August (see Fig. 11). The current vectors from the radar were used in the radar coverage area of Fig. 3c. As seen on the figure, the radar current data do not cover the region just south of the cape where strong current shears are known to exist and which can have have an important effect on the incident wave field as it travels into the area of interest from the open ocean. To extend the current grid, vectors were obtained from a finite element tidal model. The model is barotropic and run with eight tidal constituents (see Foreman et al. 1993). In agreement with the radar data, significant tidal residual currents are obtained by the model near Cape St. James. An example of a composite map is given in Fig. 11 for a time near maximum ebb flow. The strong current flowing in the southwest direction past STN295 turns sharply to the southeast in a direction parallel to the isobaths. A similar feature has been detected in the area by surface drifters (Crawford et al. 1994).

An input directional spectrum is constructed with a directional spreading function of the form $\cos^2\theta$, with a mean direction following the wind (300 deg T). For each hourly period, a total of 21 600 ray paths (60 frequency bands and 360 directions) are computed. For each component, the spectral value is obtained from (16) and the value of the incident spectrum. The equilibrium range limit is then applied for each frequency/direction component according to (18). The resulting time series of significant wave height is given in Fig. 12 along with the measurements and the previous results of the local model. The difference between the results of the local model and the results from the backward ray tracing technique is significant. Although the bathymetry effect is included in the refraction results, most of the refraction of the rays is due to the surface current because of the relatively large water depth (h > 100 m) around STN295. For each tidal cycle, a strong horizontal shear of the surface current develops when the ebb flow heading in a southwesterly direction turns to the southeast. This pronounced curvature in the current pattern strongly refracts the incident waves away from STN295, causing a decrease in wave energy despite the strong opposing current present at those times that would otherwise tend to increase the energy of the dominant waves. In this case, the refraction is strong enough to counteract the effect of the local opposing current and results in a minimum of wave energy at times of maximum local opposing current. In fact, this strong effect causes a major phase shift along with an increase in amplitude of the tidally induced oscillations in wave energy, which are now clearly in closer agreement with the measurements. Wave refraction also affects higher-frequency components and consequently the value of E_{ER}. However, in this case, the refraction-induced modulations are in phase with the results of the local model. Refraction would then reinforce E_{ER} changes due to the local current. This can explain the underestimation of the E_{ER} modulations of Fig. 10d for the first half of the study period when refraction is important.

Is this effect also present in the second half of the period? The local model results of Fig. 10b are in fact in phase with the measured wave energy modulations for this latter period, which would suggest that refraction was not effective. It is important to note that the wind direction had shifted to the west southwest after 20 August (Fig. 2). Assuming that the waves followed the wind, a simple ray tracing exercise indicates that the new direction results in a significant reduction of the wave refraction. In Fig. 13, rays for a wave component near the peak frequency of the incident wave field are presented, for the current map of Fig. 11. In the first case, the waves coming from the northwest are strongly refracted, creating a *shadow* zone of low wave energy over a region that includes STN295 (Fig. 13a). By shifting the incident wave direction to the west, the waves now reach this location with relatively little refraction (Fig. 13b). This results in a wave field at STN295 mainly controlled by changes in the local current.

4. Conclusions

A case study of wave–current interaction is presented for the Cape St. James area off the British Columbia coast. Time series of near-surface currents and wave spectra were measured by an HF radar and three Waverider buoys, respectively. A comparison between surface drifters data and concurrent radar measurements established the reliability of the radar system. The spectral wave properties measured by one of the buoys located in an area of strong tidal current show a significant variations (up to 50%) of spectral properties at the dominant tidal frequency.

In an attempt to simulate the tidally induced variations of the wave field, a local model of wave–current interaction is developed. The numerical model is based on the principle of local wave action conservation and on a universal spectral form for the equilibrium range of the wavenumber spectrum. In this local model, the problem is assumed unidirectional with all the waves traveling in the wind direction and encountering a uniform current equal to the current measured at the buoy location. Time series of the energy content of the equilibrium spectral range is obtained from both the buoy data and the local model results. Given the simplicity of the model and the complexity of the physics involved, the agreement is, for the most part, fairly good, with lower energy levels at times of strong opposing current and higher energy at times of following current.

Model predictions of the variations in significant wave height H_s were also compared with measurements. Although the magnitude of the tidally induced changes was of the same order of magnitude as the measured ones, the model results were clearly out of phase with the buoy data for the first half of the period studied. To examine the possible effect of refraction on the variations in H_s, a backward ray tracing method that included a two-dimensional form of the equilibrium spectral shape was used. Hourly current maps were produced for the area combining results from the radar and from a numerical tidal model. In the first half of the study interval, the simulated time evolution of H_s obtained from the two-dimensional model show significant differences with the local model results. It is suggested that, during this time interval, refraction effects dominate the variations in wave energy at the buoy location and account for the previously observed phase difference. In addition, it appears that, for this location, the refraction is quite sensitive to the incident wave direction as it becomes almost completely ineffective after a relatively small change in wind direction.

Acknowledgments. I thank Peter Chandler for data processing and helpful discussions, Mike Foreman for the results of the tidal model, Bill Cooke and Seaconsult Marine Research Ltd. for helping in the field work, and R. E. Thomson for comments on the manuscript. This project was supported in part by the Canadian Panel of Energy Research and Development, Project 62142.

REFERENCES

Crawford, W. R., M. J. Woodward, M. G. G. Foreman, and R. E. Thomson, 1994: Oceanographic features of Hecate Strait and Queen Charlotte Sound in summer. *Atmos.–Ocean,* in press.

Foreman, M. G. G., R. F. Henry, R. A. Walters, and V. A. Ballantyne, 1993: A finite element model for tides and resonance along the north coast of British Columbia. *J. Geophys. Res.,* **98**(C2), 2509–2531.

González, F. I., 1984: A case study of wave-current-bathymetry interactions at the Columbia river entrance. *J. Phys. Oceanogr.,* **14,** 1065–1078.

Hedges, T. S., 1987: Combinations of waves and currents: An introduction. *Proc. Inst. Civ. Eng.,* **82**(Part 1), 567–585.

——, R. G. Tickell, and J. Akrigg, 1993: Interaction of short-crested random waves and large-scale currents. *Coastal Eng.,* **19,** 207–221.

Huang, N. E., D. T. Chen, and C.-C. Tung, 1972: Interactions between steady nonuniform currents and gravity waves with applications for current measurements. *J. Phys. Oceanogr.,* **2,** 420–431.

Irvine, D. E., 1987: Extreme waves in the Agulhas—a case study of wave–current interaction. *Johns Hopkins Appl. Phys. Lab. Tech. Dig.,* **8**(1), 100–106.

——, and D. G. Tilley, 1988: Ocean wave directional spectra and wave–current interaction in the Agulhas from the shuttle imaging radar-B synthetic aperture radar. *J. Geophys. Res.,* **93**(C12), 15 389–15 401.

James, R. W., 1969: Abnormal changes in wave height. *Mariners Wea. Log,* **13,** 252–255.

Kitaigorodskii, S. A., V. P. Krasitskii, and M. M. Zaslavskii, 1975: On Phillips' theory of equilibrium range in the spectra of wind-generated waves. *J. Phys. Oceanogr.,* **5,** 410–420.

Leise, J. A., 1984: The analysis and digital signal processing of NOAA's surface current mapping system. *IEEE J. Oceanic Eng.,* **OE-9**(2), 106–113.

Liu, A. K., C. Y. Peng, and J. D. Schumacher, 1994: Wave–current interaction study in the Gulf of Alaska for detection of eddies by synthetic aperture radar. *J. Geophys. Res.,* **99**(C5), 10 075–10 085.

Phillips, O. M., 1958: The equilibrium range in the spectrum of wind-generated waves. *J. Fluid Mech.,* **4,** 426–434.

——, 1980: *The Dynamics of the Upper Ocean.* Cambridge University Press, 336 pp.

——, 1985: Spectral and statistical properties of the equilibrium range in wind-generated gravity waves. *J. Fluid Mech.,* **156,** 505–531.

Smith, R., 1976: Giant waves. *J. Fluid Mech.,* **77,** 417–431.

Smith, S. D., 1988: Coefficients for sea surface wind stress, heat flux, and wind profiles as a function of wind speed and temperature. *J. Geophys. Res.,* **93**(C12), 15 467–15 472.

Suh, K. D., Y.-Y. Kim, and D. Y. Lee, 1994: Equilibrium-range spectrum of waves propagating on currents. *J. Waterw., Port, Coastal Ocean Div.,* **111**(2), 275–288.

Teague, C. C., 1986: Multifrequency HF radar observations of currents and current shears. *IEEE J. Ocean. Eng.,* **11**(2), 258–269.

Tolman, H. L., 1991: Effects of tides and storm surges on North Sea wind waves. *J. Phys. Oceanogr.,* **21,** 766–781.

Wang, D. W., A. K. Liu, C. Y. Peng, and E. A. Meindl, 1994: Wave–current interaction near the Gulf Stream during the Surface Wave Dynamics Experiment. *J. Geophys. Res.,* **99**(C3), 5065–5079.